

# Unlocking Optical Coupling Tunability in Epsilon-Near-Zero Metamaterials Through Liquid Crystal Nanocavities

Giuseppe Emanuele Lio,\* Antonio Ferraro, Bruno Zappone,\* Janusz Parka, Ewa Schab-Balcerzak, Cesare Paolo Umeton, Francesco Riboli, Rafał Kowerdziej, and Roberto Caputo\*

Epsilon-near-zero (ENZ) metamaterials represent a powerful toolkit for selectively transmitting and localizing light through cavity resonances, enabling the study of mesoscopic phenomena and facilitating the design of photonic devices. In this experimental study, it demonstrates the feasibility of engineering and actively controlling cavity modes, as well as tuning their mutual coupling, in an ENZ multilayer structure. Specifically, by employing a high-birefringence liquid crystal film as a tunable nanocavity, the polarization-dependent coupling of resonant modes with narrow spectral width and spatial extent is achieved. Surface forces apparatus (SFA) allowed to continuously and precisely control the thickness of the liquid crystal (LC) film contained between the nanocavities and thus vary the detuning between the cavity modes. Hence, it is able to manipulate nanocavities anti-crossing behaviors. The suggested methodology unlocks the full potential of tunable optical coupling in epsilon-near-zero metamaterials and provides a versatile approach to the creation of tunable photonic devices, including bio-photonic sensors and/or tunable planar metamaterials for on-chip spectrometers.

## 1. Introduction

In the eighteenth century, the voltaic pile invented by Alessandro Volta demonstrated that stacking materials with different properties can lead to groundbreaking devices with significantly novel functionalities. Nowadays, this approach is recognized as a cornerstone of fabrication technology, particularly in the development of high-performance nano-devices. The Fabry-Perot resonator is one of the most convenient and broadly used devices in photonics, particularly for engineering light-matter coupling<sup>[1-3]</sup> and is commonly used in color filters,<sup>[4,5]</sup> two-photon direct laser writing with hyper-resolution,<sup>[6,7]</sup> optical metasurfaces,<sup>[8,9]</sup> high-heat release,<sup>[10,11]</sup> sensing devices,<sup>[12-14]</sup> and anti-counterfeiting tags,<sup>[15]</sup> just to name a few. The resonant cavity is usually fabricated by

G. E. Lio  
Physics Department  
University of Florence  
Sesto Fiorentino, Florence 50019, Italy  
E-mail: [lio@lens.unifi.it](mailto:lio@lens.unifi.it)

G. E. Lio, F. Riboli  
European Laboratory for non Linear Spectroscopy (LENS)  
Sesto Fiorentino, Florence 50019, Italy

A. Ferraro, B. Zappone, C. P. Umeton, R. Caputo  
Consiglio Nazionale delle Ricerche - Istituto di Nanotecnologia (CNR-Nanotec)  
Rende, CS 87036, Italy  
E-mail: [bruno.zappone@cnr.it](mailto:bruno.zappone@cnr.it); [roberto.caputo@unical.it](mailto:roberto.caputo@unical.it)

J. Parka, R. Kowerdziej  
Institute of Applied Physics  
Military University of Technology  
2 Kaliskiego Str., Warsaw 00-908, Poland

E. Schab-Balcerzak  
Centre of Polymer and Carbon Materials Polish Academy of Sciences  
34 M. Curie-Skłodowska Str., Zabrze 41-819, Poland

C. P. Umeton, R. Caputo  
Physics Department  
University of Calabria  
Arcavacata di Rende, CS 87036, Italy

F. Riboli  
National Institute of Optics  
CNR-INO, Sesto Fiorentino, FI 50019, Italy

R. Caputo  
Institute of Fundamental and Frontier Sciences  
University of Electronic Science and Technology of China  
Chengdu 610054, China

 The ORCID identification number(s) for the author(s) of this article can be found under <https://doi.org/10.1002/adom.202302483>

© 2023 The Authors. Advanced Optical Materials published by Wiley-VCH GmbH. This is an open access article under the terms of the [Creative Commons Attribution-NonCommercial-NoDerivs](https://creativecommons.org/licenses/by-nc-nd/4.0/) License, which permits use and distribution in any medium, provided the original work is properly cited, the use is non-commercial and no modifications or adaptations are made.

DOI: 10.1002/adom.202302483

sandwiching a transparent dielectric layer between two partially reflecting mirrors. These metal-dielectric resonators possess the intriguing properties of epsilon-near-zero (ENZ) effective permittivity<sup>[16–18]</sup> at specific resonance wavelengths that can be finely tuned by carefully selecting the thickness and refractive index of the metal and dielectric layers, and the angle and polarization of the incoming light.<sup>[2]</sup> Multilayer resonators also allow to efficiently manipulate electromagnetic waves in specific spectral ranges and enable optimal solutions for device miniaturization,<sup>[19]</sup> fabrication of perfect absorbers for structural coloring in the VIS-NIR range,<sup>[20]</sup> and high photovoltaic conversion.<sup>[21]</sup> Furthermore, photon confinement in optical nanocavities enables an efficient control of light-matter coupling in fundamental physics studies of single quantum objects<sup>[22]</sup> and correlated polaritons,<sup>[23,24]</sup> as well as applications in quantum optical devices, and sensors.<sup>[25–29]</sup>

In this context, there is high demand of devices that can be reconfigured and adapted to various emerging technologies, especially in the automotive and telecommunication sectors.<sup>[30]</sup> Current ENZ metamaterial technologies, however, lack the ability to dynamically adjust their functionalities. Liquid crystals (LCs) show a large and fast response to external stimuli and are ideal candidates to overcome this limitation. For instance, elastomeric LCs have been used to tune photonic crystals<sup>[31]</sup> and Fabry-Perot cavities.<sup>[32]</sup> LC-based metasurfaces have also been recently implemented, confirming the extraordinary capabilities of LCs in the active control of visible light,<sup>[33–36]</sup> while extensions to the microwave<sup>[37,38]</sup> and terahertz regimes<sup>[39,40]</sup> are under way. The primary challenge to developing an active, LC-based ENZ metamaterial is to reduce the LC thickness to a few hundred nanometers. This thickness is considerably smaller than the limit of a few micrometers currently achieved in display technology.

In this article, we present experimental and numerical evidence of optical coupling in ENZ multilayer metamaterials comprising a nanoscale high-birefringence LC film with tunable thickness achieved by means of a Surface Force Apparatus (SFA). Originally designed to measure surface forces across fluid films,<sup>[41]</sup> the SFA has been recently introduced in photonics as a tool to control mode coupling in optical cavities.<sup>[24,42]</sup> Specifically, we have investigated a system comprising a nanoscale LC film (T-layer) with variable thickness  $d_T$  sandwiched between two identical metal-insulator-metal (MIM) cavities, thereby creating a symmetric three-cavity resonator denoted as MIMTMIM. The MIM cavities were fabricated by sputtering deposition on two cylindrical surfaces having a radius  $R = 2$  cm. The surfaces were mounted with crossed axes in the SFA ensuring a single contact point (i.e., point of closest surface approach,  $r = 0$  in **Figure 1b**) where the surface distance was  $d_T$ . Around this point, the distance  $h_T$  varied approximately as in a sphere-plane geometry:  $h_T \approx d_T + r^2/2R$ . The three-cavity resonator was illuminated with white light under normal incidence. The SFA allowed controlling the LC thickness dynamically, accurately, and continuously from several tens of microns down to the direct mechanical contact between the MIM surfaces (**Figure 1a**). Details about the SFA technique are provided in the Experimental Section and a Scheme is shown as Supporting Information (**Figure S1**, Supporting Information).

## 2. Mode Coupling in a Multi-Cavity Resonator

Let us begin the theoretical considerations with the analysis of multi-beam interference under normal incidence in a single (Fabry-Perot) MIM cavity constituted by an isotropic material (I-layer). A plane wave resonates with a cavity if the following condition of constructive interference occurs:<sup>[43,44]</sup>

$$n_T K_q d_T = q\pi - \phi \quad (1)$$

where  $n_T$  is the refractive index of the cavity medium,  $d_T$  is the metal–metal surface separation distance,  $q$  is the resonance order,  $K_q = 2\pi/\lambda_q$  is resonance wavevector with wavelength  $\lambda_q$ , and  $\phi$  is the phase shift due to reflection at the dielectric-metal interface. Both  $n$  and  $\phi$  vary slowly with the wavelength and can be considered approximately constant across the  $\approx 100$  nm spectral range of an SFA experiment. The resonance condition Equation (1) can thus be rewritten as:

$$\lambda_q = 2n_T d_T / (q - \phi/\pi) \quad (2)$$

showing that the resonance wavelength  $\lambda_q$  increases linearly as the surface distance  $d_T$  or the refractive index  $n_T$  increases, whereas it decreases when the order number  $q$  increases. The transmittance of a MIM cavity under normal incidence can be accurately calculated as a function of wavelength  $\lambda$  and the cavity thickness using the transfer matrix multiplication (TMM) method (green lines in **Figure 1c**). For the MIM cavities considered in our experiments, only one resonance wavelength  $\lambda_1 = 560$  nm appeared in the SFA spectral range. The TMM calculation showed that  $\lambda_1$  corresponded to the first resonant mode obtained for the MIM cavity thickness of  $d_1 = 95$  nm (horizontal dashed red line in **Figure 1c**).

In a three-cavity MIMTMIM resonator, a cavity mode can overlap and interfere with the resonances of neighboring cavities across the metal (M) layers. Consequently, the coupling of resonances and the optical interaction among the cavities that give rise to hybrid resonance modes.<sup>[42]</sup> A three-cavity resonator with a variable thickness  $d_T$  of the central cavity (T-layer) and fixed thickness  $d_1$  of the outer cavities (I-layers) resonates at three different wavelengths ( $\lambda_L$ ,  $\lambda_1$ , and  $\lambda_U$  in **Figure 1c**), related to the resonances of the three cavities. The dispersion of a symmetric three-cavity resonator has been studied in detail in ref. [42] and will be discussed in Section IV. Briefly, the dependence of the wavelength triplet ( $\lambda_L$ ,  $\lambda_1$ , and  $\lambda_U$ ) on  $d_T$  reflects the hybridization and avoided crossing between equal-symmetry modes of the inner and outer cavities. Namely, the avoided-crossing point corresponds to the thickness  $d_T$  at which the inner cavity should resonate at the same wavelength  $\lambda_1$  as the outer cavities. Interestingly,  $\lambda_L$  and  $\lambda_U$  depend on  $d_T$ , whereas  $\lambda_1$  is constant. Far from the avoided-crossing point,  $\lambda_L$  is close to the resonant wavelength of the inner cavity, while  $\lambda_U$  is close to the constant wavelength  $\lambda_1$ , or vice versa. Therefore,  $\lambda_L$  or  $\lambda_U$  increases almost linearly with the inner cavity thickness following Equation (1).

Because resonance modes sense both cavity thickness and refractive index, filling the inner cavity with a birefringent LC material leads to the doubling of resonance modes (e.g.,  $\lambda_{Lo}$  and  $\lambda_{Le}$  for the ordinary and extraordinary polarization, respectively, **Figure 1c**). These preliminary considerations highlight the

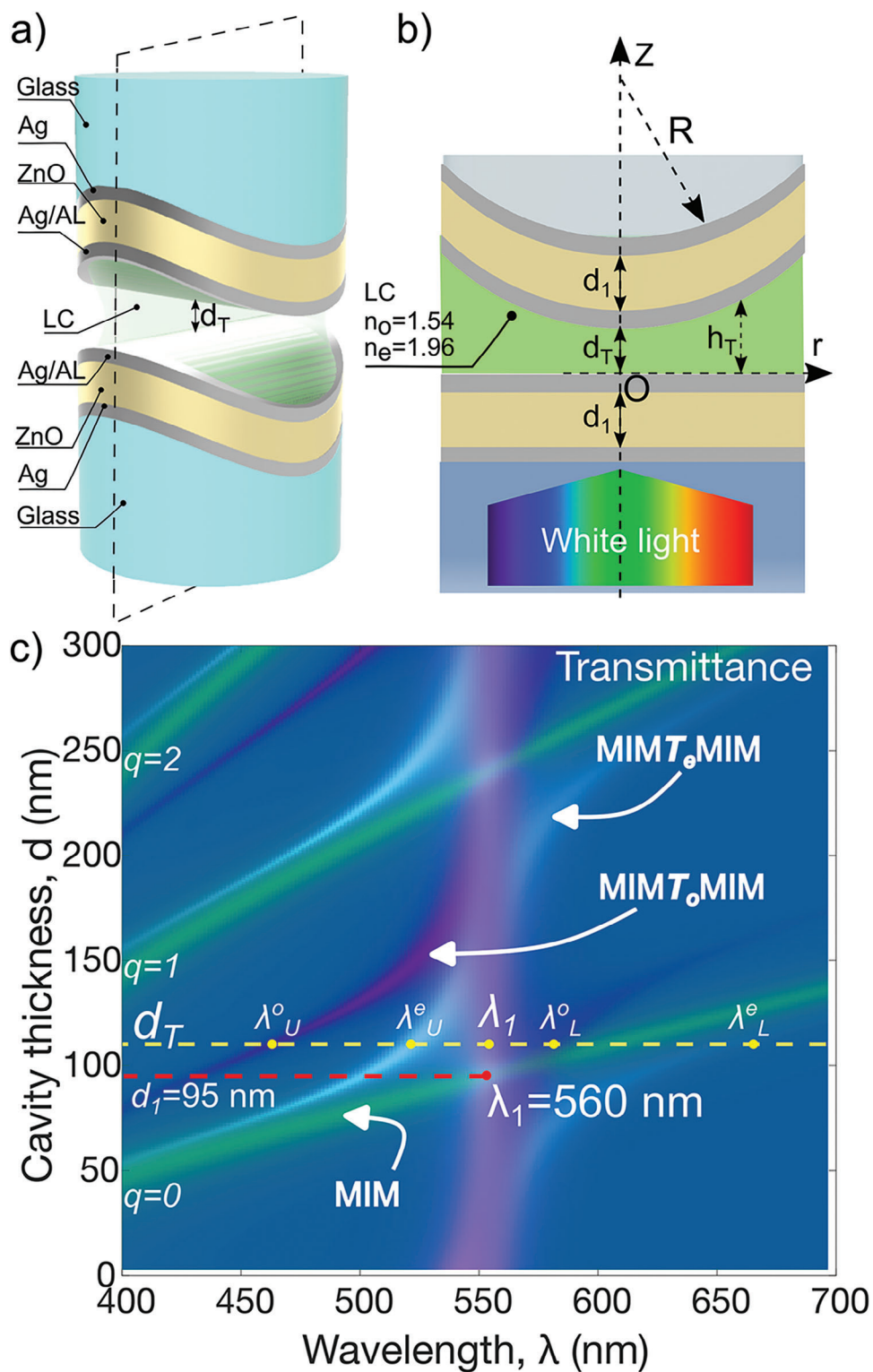


**Figure 1.** a) Illustration of the three-cavity MIMTMIM resonator realized in the SFA. A ZnO layer (I) sandwiched between two Ag layers (M) with equal thickness constitutes a MIM cavity and was deposited by sputtering on each of the two cylindrical glass lenses of the SFA. LC film (T) confined between the MIM cavities forms a third cavity with non-uniform thickness. b) Cross-section view of the SFA geometry with the  $z$  direction of light incidence is evidenced. The geometry of the two cylindrical surfaces is approximated by a plane and a sphere with  $r$  being the lateral distance from the contact point ( $r = 0$ ).  $h_T$  and  $d_T$  are respectively the surface distances at a given  $r$  and at  $r = 0$ . c) Transmittance under normal incidence calculated using the TMM method for a MIM cavity (green lines) as a function of the wavelength  $\lambda$  and thickness of the I-layer, and for the three-cavity resonator as a function of  $\lambda$  and thickness  $d_T$  of the LC film (T-layer), for both ordinary (MIMT<sub>o</sub>MIM, purple curves) and extraordinary polarizations (MIMT<sub>e</sub>MIM, cyan curves). A resonance corresponds to a local intensity maximum.  $\lambda_1$  is the first-mode wavelength of the MIM cavity obtained for the thickness  $d_1$ . In addition to  $\lambda_1$ , four different wavelengths  $\lambda_{U,L}^{o,e}$  are obtained at the LC thickness  $d_T$  marked with a yellow horizontal line, where  $o$  and  $e$  indicate the given polarization and  $U$  and  $L$  denote the (lower/upper) photon energy relative to  $\lambda_1$ .

potential of birefringent materials for tuning the resonances of metal-dielectric metamaterials. On the other hand, when the T-layer is an optically anisotropic LC film, these wavelengths depend on light polarization (purple and cyan curves in Figure 1c).

### 3. Experimental Results

In the realized system, the thickness of silver (Ag, M-layers) and zinc oxide (ZnO, I-layers) is 30 and 95 nm, respectively. The LC material considered for the T-layer is a high-birefringence nematic liquid crystal mixture named LC1825, synthesized by the Military University of Warsaw<sup>[45]</sup> with a birefringence of  $\Delta n = n_e - n_o = 0.42$ , where  $n_e = 1.96$  and  $n_o = 1.54$  are the extraordinary and ordinary refractive indices at room temperature, respectively. The photoalignment compound JK158<sup>[46]</sup> was spin-coated on the Ag surfaces facing the LC to induce planar orientation along the cylinder axis on one surface and perpendicular to the axis on the other surface. Crossing the axes in the SFA ensured a planar alignment uniform across the LC thickness. Therefore, polarized parallel or perpendicular to the LC orientation travelled in the LC film as purely extraordinary or ordinary waves, respectively. Further details on the fabrication and materials used in our experiments are provided in the Experimental Section. During the experiment, a collimated white-light beam coming from a halogen lamp illuminated the MIMTMIM resonator under normal incidence and the transmitted intensity was analyzed using an imaging spectrograph coupled to a high-resolution CCD camera. In the spectrogram of Figure 2, the transmitted intensity  $I$  was measured as a 2D function of the wavelength  $\lambda$  and lateral distance  $r$  for the contact point ( $r = 0$  in Figure 1). A resonance produces a local maximum in the intensity function  $I_0(r, \lambda)$ . Because  $h_T \approx d_T + r^2/2R$  around the contact point, resonance wavelengths that depend linearly on  $h_T$  vary quadratically with  $r$  and create curved fringes in the SFA spectrograms with a parabolic tip corresponding to the contact point. In the spectrogram of Figure 2b, the intensity was measured at the contact position ( $r = 0$ ) while increasing the surface distance  $d_T$  at a constant speed  $u$  of a few  $\text{nm s}^{-1}$  using a motorized actuator (Figure 1). In this case, the intensity  $I_0$  was resolved as a 2D-function of  $\lambda$  and time. Because  $d_T(t) = d_0 + ut$ , where  $d_0$  is the initial thickness, each vertical line in the spectrogram corresponds to a specific time  $t$  and surface distance  $d_T(t)$ . The advantage of this approach is that the SFA can vary  $d_T$  dynamically and continuously over a wide range of surface distances, from several  $\mu\text{m}$  to direct surface contact ( $d_T < 1$  nm for molecularly smooth surfaces), with an accuracy better than 1 nm and execution time of the order of minutes. To vary  $d_T$ , the surfaces were approached to or separated from each other at a constant speed. By recording  $I_0(\lambda, t)$ , the SFA allowed studying the

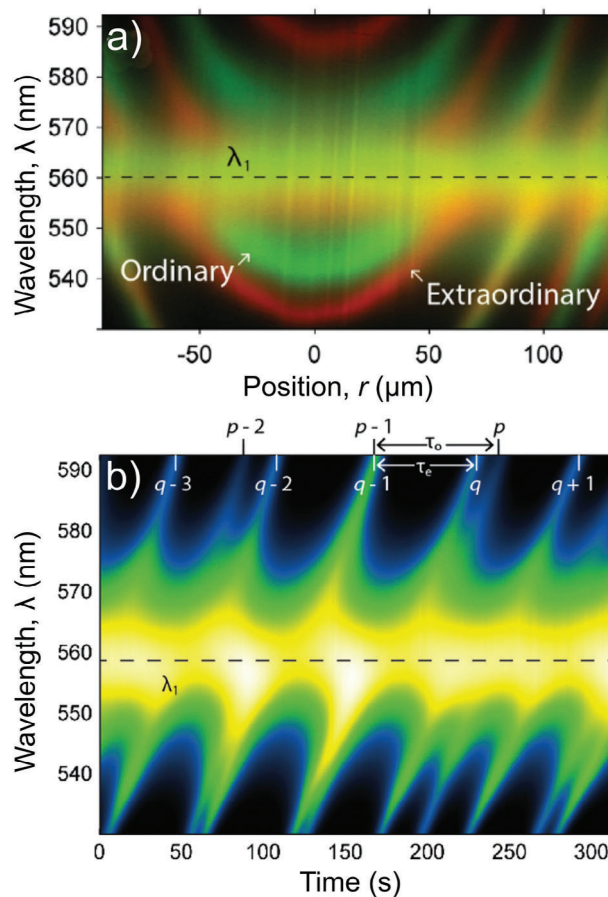


**Figure 2.** a) Transmitted intensity  $T$  measured for the MIMTMIM resonator in the SFA as a function of the wavelength  $\lambda$  and lateral distance  $r$  from the surface contact position ( $r = 0$ ). Green and red fringes correspond to ordinary and extraordinary polarization, respectively, and were obtained by setting a linear polarizer perpendicular or parallel to the planar LC anchoring direction. The two fringe types overlap in the yellow regions, corresponding to the first-order resonance wavelength  $\lambda_1$  of the MIM cavities. b) Transmitted intensity measured at the contact position ( $r = 0$ ) as a function of time  $t$  and wavelength  $\lambda$  while separating the surfaces at constant speed  $u$ . Each value of  $t$  corresponds to a different separation distance (i.e., LC film thickness):  $d_T = d_0 + ut$ , where  $d_0$  is the initial surface separation and  $u$  is the (constant) speed of surface separation. The mode order for ordinary and extraordinary fringes is denoted as  $q$  and  $p$ , respectively. A fringe with order  $q$  (or  $p$ ) exits the spectral range at wavelength  $\lambda = 593.2$  nm after a time  $\tau$  compared to the fringe with order  $q - 1$  (or  $p - 1$ ). The delay is  $\tau_o = 78.35$  s and  $\tau_e = 60.85$  s for ordinary and extraordinary fringes, respectively.



resonance dispersion as a function of the cavity thickness  $d_T$  in a single sweep of thickness, instead of fabricating multiple cavities with different thicknesses. In the spectrograms of Figure 2a,b, the first-order resonance of the fixed-thickness MIM cavities produces a specific resonance wavelength  $\lambda_1$  that does not depend on the thickness ( $d_T$  or  $h_T$ ) of the MTM cavity, i.e., the LC film. On the other hand, the other fringes in the spectrogram are due to resonances of the MTM cavity and, therefore, depend both on the film thickness and polarization of the incident light. For a fixed surface distance ( $d_T$  or  $h_T$ ) and far from  $\lambda_1$ , these fringes show an approximately parabolic shape (Figure 2a) reflecting the surface curvature, as expected. Due to the LC birefringence, these fringes form two distinct sets that can be separately extinguished using a linear polarizer parallel or perpendicular to the planar anchoring direction, as shown in Figure 2a (see also an example of unpolarized spectrogram in Figure S2, Supporting Information). This finding demonstrates that the resonance modes of the MTM cavity are linearly polarized along the ordinary and extraordinary axis of the uniformly aligned LC. The extraordinary modes appear slightly brighter than the ordinary ones (Figure S2, Supporting Information), because light was directed into the spectrograph using a right-angle mirror with polarization-dependent reflectivity (Figure S1, Supporting Information). This allows to identify the fringe polarization even though we cannot use a polarizer to dynamically resolve the polarization while varying  $d_T$ . Figure 2b shows that extraordinary fringes enter and exit the spectral range of the SFA (at a wavelengths distant from  $\lambda_1$ ) more rapidly than ordinary fringes. In the entrance and exit regions, resonances approximately follow Equation (1). Therefore, if the mode with order  $q$  resonates at a given wavelength  $\lambda_1$ , then the mode with order  $q \pm r$  resonates at the same wavelength after displacing the surfaces by a distance  $\Delta d = \pm r\lambda_1/2n$ . As a result of the inequality  $n_e > n_o$ , extraordinary fringes with index  $n_e$  cross the wavelength  $\lambda_1$  more often than ordinary fringes as the distance  $d_T$  is increased. If the surfaces are separated at a constant speed  $u$ , the fringe with order  $q$  exits the spectral range after a time  $\tau = \Delta d/u$  compared to the fringe with order  $q - 1$ . Figure 2b shows ordinary fringes exiting the spectral range at wavelength 593.2 nm at periodic time intervals  $\tau_o = 78.3$  s, whereas the period is  $\tau_e = 60.8$  s for extraordinary fringes. The ratio of these two periods,  $\tau_o/\tau_e = 1.29$ , is in good agreement with the value  $\tau_o/\tau_e = n_e/n_o = 1.27$  predicted by Equation (1) using the nominal refractive indices (at room temperature)  $n_e = 1.96$  and  $n_o = 1.54$  of the LC. **Figures 3a,b** show intensity spectrograms  $I_0(\lambda, t)$  obtained for the ordinary and extraordinary polarization, respectively, by using a polarizer in transmission. Resonance wavelengths are highlighted by black dashed lines and are referred to as  $\lambda_1$ ,  $\lambda_U$ , and  $\lambda_L$ . As the thickness  $d_T$  of the LC film increases,  $\lambda_U$  approaches  $\lambda_1$  while  $\lambda_L$  departs from  $\lambda_1$ . Eventually,  $\lambda_U$  and  $\lambda_L$  become equally spaced from  $\lambda_1$  by a distance  $\Omega$ . This behavior agrees with the numerical prediction and demonstrates the possibility of dynamically tuning the modes at different wavelengths ranging from 530 to 590 nm by acting on LC thickness or incoming light polarization. The MIMTMIM system studied in this work presents ENZ resonances for both LC thicknesses (134 and 100 nm) and refractive indices ( $n_o$  and  $n_e$ ). This is confirmed by the effective dielectric constant that has been evaluated using the effective medium theory (EMT),<sup>[47]</sup> as reported in Figure S3 (Supporting Information). Moreover, the phase after propagation (through the whole

resonator) was found to be  $\phi \rightarrow 0$  meaning that  $n \rightarrow 0$  at the resonant wavelengths as shown in Figure S3 b,d, Supporting Information). It is also important to note that when the phase goes toward zero, the phase velocity becomes infinite, indicating that the electromagnetic wave “tunnels” through ENZ material, enabling high transmission.<sup>[18,48]</sup>

#### 4. Tuning Mode Coupling via LC Confinement and Reorientation

In order to understand why mode coupling produces a wavelength triplet, we calculated the transmitted intensity as a function of wavelength  $\lambda$  and LC film thickness  $d_T$  using the TMM method (Figure 4a), and selected three different values of  $d_T$  to compute, by a finite element method (COMSOL), the electric field map along the direction perpendicular to the MIMTMIM resonator as a function of  $\lambda$  and  $z$  position<sup>[21]</sup> (Figure 4b–e).

For  $d_T = 100$  nm and ordinary polarization (Figure 4b), the high-energy mode has wavelength  $\lambda_U^o \approx 450$  nm and is farther away from  $\lambda_1$  than the low-energy mode with wavelength  $\lambda_L^o \approx 585$  nm. This unequal wavelength spacing is reflected in mode hybridization. Namely, the high-energy mode is mainly located in the central MTM cavity while the low-energy mode is more delocalized among the central and outer (MIM) cavities. When the LC film thickness is increased to  $d_T = 134$  nm (Figure 4c), the high-energy wavelength (Figure 4c)  $\lambda_U^o \approx 510$  nm and low-energy wavelength  $\lambda_L^o \approx 620$  nm are almost equally spaced from  $\lambda_1$  and show a comparable degree of delocalization. When the LC film thickness is further increased to  $d_T = 160$  nm (Figure 4d), the situation shown in Figure 4b is reversed and the high-energy mode at  $\lambda_U^o \approx 530$  nm is closer to  $\lambda_1$  and more delocalized than the low-energy mode at  $\lambda_L^o \approx 670$  nm. Mode hybridization in MIMTMIM resonator can be understood based on its mirror symmetry under reflection on the middle plane of the central T-cavity. Symmetry requires that resonances be either even (+) or odd (-) under reflection (Figure 4b–e). Using first-order perturbation theory or variational method,<sup>[42,49]</sup> these modes can be approximated as symmetry-adapted linear combinations of single-cavity modes. In particular, the field  $E_c$  of first-order mode in the central cavity is even and, therefore, hybridizes with the field  $E_+$  of the even combination of outer-cavity modes. Against, the odd combination  $E_-$  cannot hybridize with an even mode such as  $E_c$ . While the modes  $E_c$  and  $E_+$  overlap and interfere with each other, particularly within the metal layers of the central MTM cavity, direct overlap and interference between the outer cavities is negligible and, as a result, the wavelength  $\lambda_-$  of the  $E_-$  mode is very close to the wavelength  $\lambda_1$  of an isolated MIM cavity. Indeed, the difference between  $\lambda_-$  and  $\lambda_1$  was too small to be detected in our experiments.

Hybridization between same-parity modes produces the wavelengths  $\lambda_L$  and  $\lambda_U$  observed both in the SFA experiments and in our calculation.<sup>[42]</sup> For first-order modes, these wavelengths correspond to the modes  $E_L = E_c + \alpha E_+$  and  $E_U = E_c - \beta E_+$ , respectively, where the positive linear coefficients  $\alpha$  and  $\beta$  depend on the thickness  $d_T$  of the central MTM cavity. The wavelengths  $\lambda_L$  and  $\lambda_U$  are due to the anti-crossing interaction between the even mode  $E_c$  and  $E_+$  occurring as  $d_T$  varies (Figure 4b,d). Namely, the  $E_U$ -mode repels the  $E_L$ -mode as it moves toward lower energies, while the  $E_-$  mode is unaffected. The avoided-crossing point is

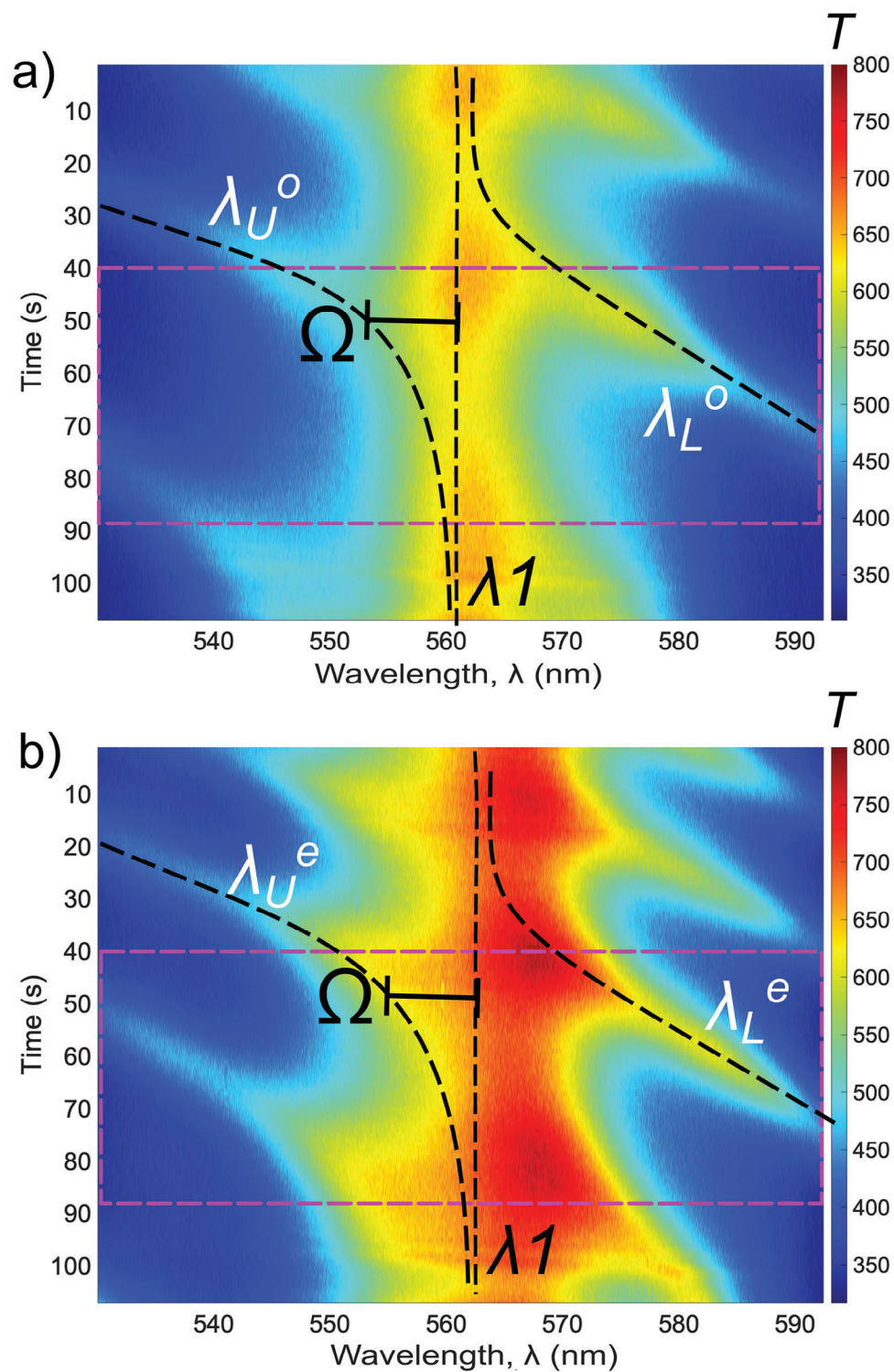


**Figure 3.** Light intensity  $T$  transmitted through the system measured for a) ordinary and b) extraordinary polarizations as a function of the wavelength  $\lambda$  and time  $t$  during surface separation (LC cavity expansion) with constant surface speed  $u$ . The maps show the resonance wavelengths  $\lambda_U$  and  $\lambda_L$  obtained during the surface separation together with their separation  $\Omega$  from the resonance  $\lambda_1$ .

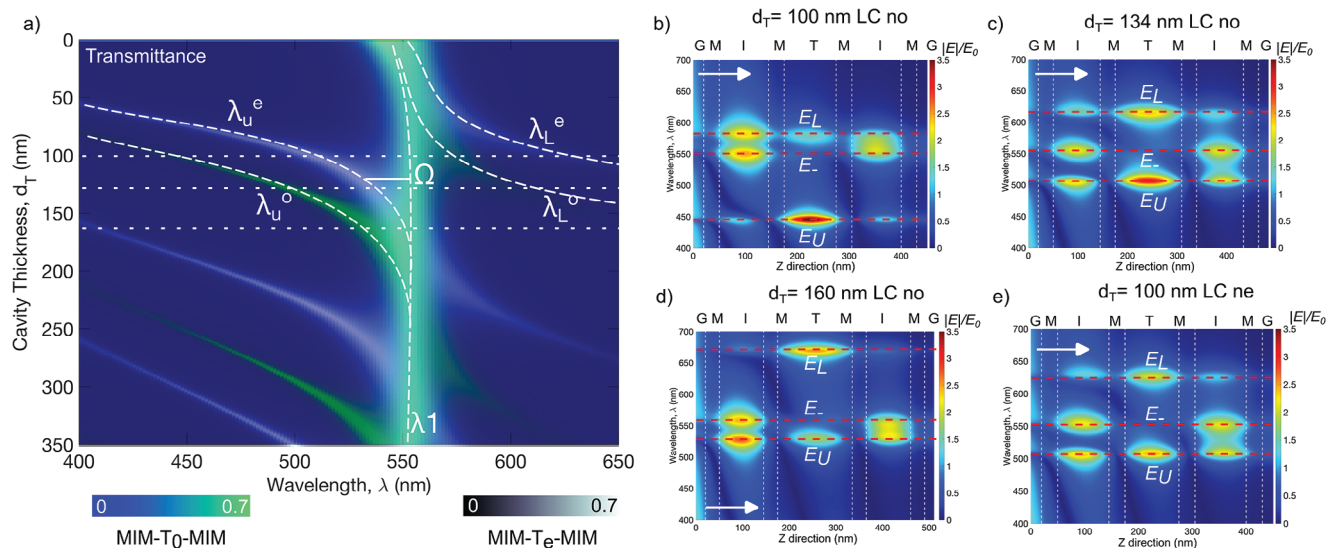


**Figure 4.** a) Calculated spectrogram showing the transmitted intensity as a function of the wavelength  $\lambda$  and of the LC cavity thickness  $d_T$  for both ordinary (blue-to-green colormap in the bottom left corner) and extraordinary polarizations (black-to-dark cyan colormap in the bottom right corner). b,d) Normalized electric field amplitude ( $|E|/E_0$ ) calculated for the ordinary polarization (LC<sub>no</sub>) as a function of the position  $z$  along the surface normal of the MIMTMM resonator and wavelength  $\lambda$ . The considered cavity thickness  $d_T$  is indicated above each image. e) Electric field calculated for  $d_T = 100$  nm and extraordinary polarization (LC<sub>ne</sub>). The white dotted vertical lines mark the metal-dielectric interfaces, G (glass) is the medium outside the resonators. The white arrow shows the direction of incidence.

reached when the wavelength  $\lambda_q$  of the  $E_c$ -mode (Equation (1)) overlaps with the first-order wavelength  $\lambda_1$  of the outer MIM cavities. In other words, the difference or “detuning” between the photon energies of the two modes becomes zero. At this point, the modes  $E_L$  and  $E_U$  become uniformly delocalized across the resonator, with equal intensity maxima in each cavity ( $\alpha, \beta \approx 1$ , Figure 4c). At the avoided-crossing point, the wavelengths  $\lambda_L$  and  $\lambda_U$  are found at an equal distance  $\Omega$  from the wavelength  $\lambda_1$  of the  $E_-$  mode.

A decisive advantage of using an anisotropic LC film is that the detuning can be actively controlled not only by varying the MTM cavity thickness, but also by selecting the refractive index of the LC. This fact is highlighted in Equation (1) showing that the resonance wavelength  $\lambda_q$  depends on the product  $n_T d_T$  and, therefore, the thickness  $d_T$  and index  $n_T$  play equivalent roles. For example, the transmittance variation obtained by increasing the film thickness from  $d_T = 100$  nm (Figure 4b) to  $d_T = 134$  nm (Figure 4c) can also be obtained by switching the refractive index from ordinary to extraordinary (Figure 4d) while keeping the film thickness fixed to  $d_T = 100$  nm. The switching can be obtained by changing the polarization from ordinary to extraordinary, or acting on the LC orientation (e.g., by applying a voltage to the silver surfaces of the MTM cavity) so as to vary the refractive index seen by extraordinary waves.

As a further demonstration of mode hybridization, the electric field was calculated using finite element method for the three LC thicknesses under normal incidence in Figures S4 and S5 (Supporting Information) the transmittance plots, electric field confinement into the LC cavity ( $n_c$ ), and electric field distributions along the propagation direction are also shown.

In Figure 5a, the wavelength splitting  $2\Omega$  related to the difference  $\lambda_L - \lambda_U$ ,  $\lambda_1 - \lambda_U$  and  $\lambda_1 - \lambda_L$  is shown as a function of the LC thickness. The top and bottom panels show the resonance

wavelengths retrieved via a multiple Gaussian fit on the transmittance curves, for the anti-crossing behavior represented by  $\lambda_U$  approaching  $\lambda_L$ ,  $\lambda_U$  approaching  $\lambda_1$ , and  $\lambda_1$  approaching  $\lambda_L$ , for the ordinary and extraordinary LC refractive index, respectively. The minimum value of  $2\Omega$  corresponds to the avoided-crossing point and maximum coupling between same-parity modes. The same behavior is observed in experiments (Figure 5b). The slight difference related to the amplitude ( $2\Omega$ ) reported in both plots, numerical and experimental ones, for extraordinary polarization is a consequence of the non negligible effect of changing the surrounding medium around the two MIM resonators. In Supporting Information, we also simulated the angular dependence by varying the incident angle  $\theta_i$  from  $0^\circ$  to  $80^\circ$  in steps of  $2^\circ$  for both ordinary and extraordinary polarization (Figure S6, Supporting Information). The results show that the three-cavity resonator is not significantly perturbed by the variation of the incident angle, especially for the extraordinary polarization.

## 5. Conclusion

In conclusion, we presented a detailed study on how to design and actively tune strongly confined hybrid modes in 1D layered structures working in visible wavelengths. The active control is enabled by a high-birefringence LC in combination with an SFA that can vary the cavity thickness rapidly, continuously, and accurately from several  $\mu\text{m}$  down to direct contact between its metal mirror surfaces. Importantly, we studied numerically and experimentally how the system performs in terms of weak and strong light coupling conditions when an LC film is confined between two MIM cavities. This result has significant practical implications for the development of innovative devices as it enables the possibility to excite multiple resonant modes across the LC cavity. This is of fundamental importance for developing



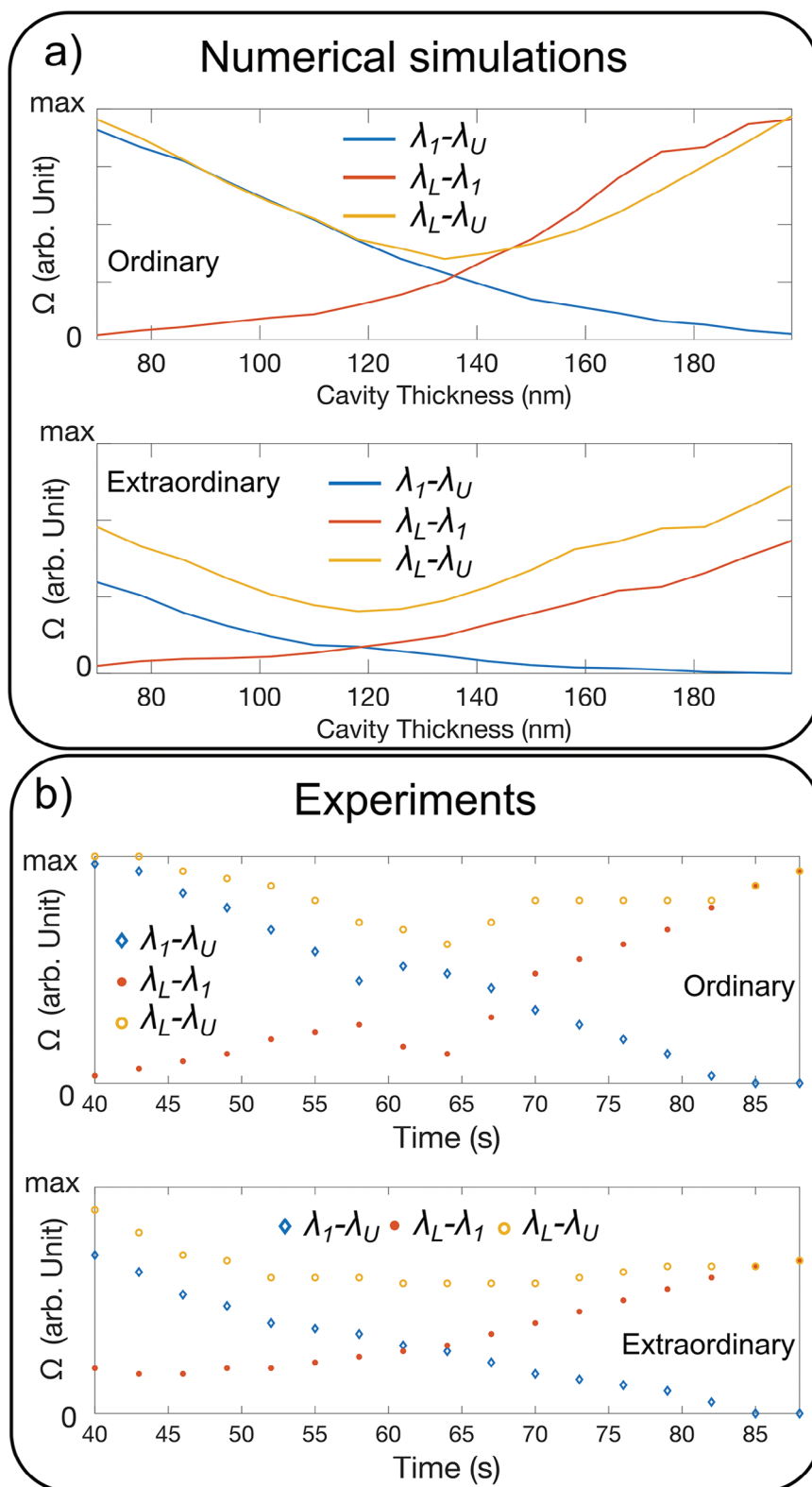


**Figure 5.** a) Numerical and b) experimental distance  $2\Omega$  between the wavelengths  $\lambda_L$  and  $\lambda_U$  for ordinary (top panels) and extraordinary (bottom panels) polarizations calculated for the following resonant mode conditions:  $\lambda_U$  approaches  $\lambda_1$ ,  $\lambda_L$ , departs from  $\lambda_1$  and  $\lambda_U$  approaches  $\lambda_L$  (anti-crossing).



active and reconfigurable devices that can find applications as a platform for optical beam steering devices. Thanks to the tunability of these photonic modes, the proposed system can be of extremely high importance for bio-sensing where it is necessary to involve high energy modes (short wavelengths, from 450 to 530 nm) excitable in free-space. Although the cavity resonances were obtained under normal incidence, it is expected that plasmonic modes can also be excited in a multi-cavity metamaterials under oblique incidence, notably without using any coupler (i.e., a grating) to generate evanescent waves. To this end, the SFA could be used to study the generation, coupling, and transmission of plasmonic modes in multi-cavity metamaterials as a function of the thickness and refractive index of LC loaded cavity.

## 6. Experimental Section

**Sample Fabrication:** The MIM cavities were fabricated by DC/RF sputtering (model Kenosistec KC300C), and they were constituted of Ag and transparent Zinc-oxide (ZnO), respectively with target thickness of 30 and 95 nm, on cylindrical glass lenses. The lenses had a diameter of  $R = 2$  cm, the thickness of 4 mm, 60/40 scratch/dig surface quality, centration wedge angle  $< 5$  arcmin, and irregularity (interferometer fringes)  $\lambda/2$  at a wavelength of 630 nm. Ag was chosen for its large extinction coefficient  $k > 1 \gg n$ , ensuring a high reflectivity and an approximately real negative permittivity in the metal layers while ZnO was chosen for its transparency ( $n > 1 \gg k$ ). For the deposition, the following parameters were used: vacuum  $7 \cdot 10^{-6}$ , DC power 100W for 62s for Ag layer while ZnO were deposited using the RF cathode at a power of 80W and time of 31min 36s. In order to align the LC layer, a solution photo-active poly(amide imide), denominated JK158 in N-methylpyrrolidone (1 wt.%) was spin-coated on top of the exposed Ag layers at 3500 rpm for 45 s followed by a baking a 65°C for 3 h to evaporate the solvent. Finally, the JK158 film was irradiated through a linear polarizer with a light source having wavelength of 365nm (UV-Kub 2, KLOE') for 30 min. The poly(amide imide) was described in ref. [50]. JK158 contains randomly aligned azo-dye molecules that reorient perpendicularly to the polarization direction of UV light to minimize the absorption cross-section. The LCs in contact with the aligned JK158 molecules acquire the same alignment.

**The Surface Forces Apparatus:** A surface forces apparatus (SFA) Mark III by Surface LLC, USA was used for the experiments.<sup>[42,51]</sup> One of the MIM-coated cylindrical lenses was fixed on a rigid support, whereas the other was attached to the free end of a double cantilever spring. The opposite end was rigidly attached to a motorized precision actuator performing controlled displacements with a known uniform speed  $u$  of a few  $\text{nm s}^{-1}$ . A LC droplet with a volume of 50  $\mu\text{L}$  was infiltrated between the surfaces by capillarity.

Transmission spectra were obtained by illuminating the surfaces under normal incidence with white light from a halogen lamp. The transmitted light was collected through the entrance slit of an imaging spectrograph (PI Acton Spectra Pro 2300i) aligned with one of the cylindrical lenses and recorded with a high-sensitivity CCD camera (Andor Newton DU940P-FI).

The separation distance between the crossed cylindrical surfaces, equal to the LC film thickness, was  $h_T \approx d_T + r^2/2R$ , where  $r$  was the lateral distance from the surface contact position ( $r = 0$ ),  $d_T$  was the surface distance at the contact position, and  $R = 2$  cm was the cylinder radius (Figure 1a,b). The film thickness  $h_T$  depended on  $r$  as in a sphere-plane geometry because the camera probed a small surface region surrounding the contact position, such that  $r \leq 0.15$  mm  $\ll R$ .<sup>[52]</sup>

The SFA provided a passive geometry-based method and an active displacement-based method for studying the effects of film thickness variations. In the passive method, the surfaces were kept at a constant surface distance  $d_T$ . The CCD camera recorded the transmitted intensity as a 2d function  $I(\lambda, r)$  of the wavelength  $\lambda$  and distance  $r$  along the spectrograph entrance slit. Because the dependence of  $h_T$  on  $r$  was known, intensity vari-

ations along the  $r$ -axis could be immediately related to known variations of  $h_T$ . The image in Figure 2a is a 2d spectrogram produced with this method.

In the active method, the CCD records a video with acquisition rate of (1–3) images per second while varying the surface distance  $d_T$  at a constant speed. The intensity spectrum  $I(\lambda, 0)$  at the contact position was selected from each image, and the spectra were stacked in 2d spectrogram  $I(\lambda, t)$ , where  $t$  is the spectrum acquisition time. The spectrogram in Figures 2b was obtained with this method. In both methods, resonances due to constructive multi-beam interference within the cavities appeared as intensity peaks in the spectrograms, i.e., local maxima of 2d intensity functions.

Before starting a measurement, the SFA was equilibrated for at least 1 h at 25.0 °C to reduce unwanted thermal or mechanical drifts of the distance  $d_T$  below 5  $\text{nm min}^{-1}$ . To obtain uniform  $d_T$  variations, the fixed cantilever end was displaced at a controlled speed of a few  $\text{nm s}^{-1}$  using a motorized precision actuator. Because the surfaces were well separated from each other and did not interact mechanically, the cantilever moved without deflecting and, therefore, the distance  $d_T$  varied by an amount equal to cantilever displacement.

**Numerical Simulations:** The transfer matrix method (TMM) analysis were performed using a script implemented in commercial software Matlab. It uses as input the refractive indices data, the layer thicknesses and it allows calculating the spectrum varying the T cavity thickness. The refractive indices of Silver and Zinc Oxide were retrieved with Woollam M2000 ellipsometer. They were already reported in the supporting Information of the previous manuscript including a link to an open repository of such data.<sup>[14]</sup>

Finite Element Method (FEM) simulation were performed using COMSOL Multiphysics with the same scheme reported in ref. [2]. In order to analyze the electric field  $|E|/E_0$ , where  $E_0$  had been calculated as  $E_0 = \sqrt{(P/w)Z_0}$ , here  $P$  is the input power ( $1 \text{ W m}^{-2}$ ),  $w$  represents the area illuminated by the light beam and  $Z_0$  is the impedance, in the MIMTMIM system a 1D cutting line had been used to collect the normalized electric field as function of the structure size and wavelengths. The cutting line had been chose to cover the entire length of the MIMTMIM system plus extra 20 nm in the glass before and after the structure.

## Supporting Information

Supporting Information is available from the Wiley Online Library or from the author.

## Acknowledgements

This research was performed in the framework of the bilateral (Italy-Poland) project: "Active metamaterials based on new generation liquid crystals (LCMETA)" funded by the Italian Ministry of Foreign Affairs and International Cooperation and the Polish National Agency for Academic Exchange NAWA. G.E.L and F.R. thank the FASPEC (Fiber-Based Planar Antennas for Biosensing and Diagnostics) - supported by Tuscan region in the Horizon 2020 framework - and the project "Complex Photonic Systems (DFM.AD005. 317)". G.E.L. also thanks the research project "FSE-REACT EU" financed by National Social Fund - National Operative Research Program and Innovation 2014-2020 (DM 1062/2021). A.F and R.C thank the project "DEMETRA – Sviluppo di tecnologie di materiali e di tracciabilità per la sicurezza e la qualità dei cibi" PON ARS01 00401. R.K. and J.P. acknowledged the financial support from the MUT University Grant UGB 22 804 from funds for year 2023.

## Conflict of Interest

The authors declare no conflict of interest.

## Author Contributions

G.E.L. and A.F. contributed equally to this work and wrote the article. G.E.L. and R.C. conceived the main idea in the framework of the research project "LCMETA". G.E.L. and A.F. performed numerical simulations and samples fabrication. B.Z. performed the SFA measurements and provided theoretical explanations. E.S.-B. synthesized and delivered LC photoaligning materials and supported the work with fundamental technical advice. R.K. tested photo-aligning materials. J.P., R.K., C.P.U., F.R., and R.C. provided fundamental support thanks to their expertise in liquid crystals. F.R. provided his expertise on light coupling behavior in complex media to explain the physics behind this work. All authors revised the paper and accepted its contents.

## Data Availability Statement

The data that support the findings of this study are available from the corresponding author upon reasonable request.

## Keywords

ENZ, high-birefringence liquid crystal, liquid crystals, metamaterials, nano optical-cavities

Received: October 23, 2023  
Published online: November 27, 2023

- [1] F. Réveret, P. Disseix, J. Leymarie, A. Vasson, F. Semond, M. Leroux, J. Massies, *Phys. Rev. B* **2008**, *77*, 195303.
- [2] G. E. Lio, G. Palermo, R. Caputo, A. De Luca, *RSC Adv.* **2019**, *9*, 21429.
- [3] J. Cao, S. De Liberato, A. V. Kavokin, *New J. Phys.* **2021**, *23*, 113015.
- [4] S. M. Choudhury, A. Shaltout, V. M. Shalaev, A. V. Kildishev, A. Boltasseva, in *CLEO: QELS Fundamental Science*, Optical Society of America, Washington, DC **2016**, pp. FF1D–8.
- [5] G. E. Lio, A. Ferraro, M. Giocondo, R. Caputo, A. De Luca, *Adv. Opt. Mater.* **2020**, *8*, 2000487.
- [6] Z. Guo, H. Jiang, K. Zhu, Y. Sun, Y. Li, H. Chen, *Phys. Rev. Appl.* **2018**, *10*, 064048.
- [7] G. E. Lio, A. Ferraro, R. Ritacco, D. M. Aceti, A. De Luca, M. Giocondo, R. Caputo, *Adv. Mater.* **2021**, *33*, 2008644.
- [8] A. M. Shaltout, N. Kinsey, J. Kim, R. Chandrasekar, J. C. Ndukaife, A. Boltasseva, V. M. Shalaev, *Proc. IEEE* **2016**, *104*, 2270.
- [9] R. Kowrdziej, A. Ferraro, D. C. Zografopoulos, R. Caputo, *Adv. Opt. Mater.* **2022**, *10*, 2200750.
- [10] P. N. Dyachenko, S. Molesky, A. Y. Petrov, M. Störmer, T. Krekeler, S. Lang, M. Ritter, Z. Jacob, M. Eich, *Nat. Commun.* **2016**, *7*, 1.
- [11] A. Ferraro, G. E. Lio, A. Hmina, G. Palermo, J. M. Djouda, T. Maurer, R. Caputo, *Nanophotonics* **2021**, *10*, 3907.
- [12] K. V. Sreekanth, Y. Alapan, M. ElKabbash, E. Ilker, M. Hinczewski, U. A. Gurkan, A. De Luca, G. Strangi, *Nat. Mater.* **2016**, *15*, 621.
- [13] K. V. Sreekanth, S. Zeng, K.-T. Yong, T. Yu, *Sens. Actuators, B* **2013**, *182*, 424.
- [14] G. E. Lio, A. Ferraro, R. Kowrdziej, A. O. Govorov, Z. Wang, R. Caputo, *Adv. Opt. Mater.* **2023**, *11*, 2203123.
- [15] A. Ferraro, G. E. Lio, M. D. L. Bruno, S. Nocentini, M. P. De Santo, D. S. Wiersma, F. Riboli, R. Caputo, R. C. Barberi, *Adv. Mater. Technol.* **2022**, *8*, 2201010.
- [16] S. Vassant, J.-P. Hugonin, F. Marquier, J.-J. Greffet, *Opt. Express* **2012**, *20*, 23971.
- [17] O. Reshef, I. De Leon, M. Z. Alam, R. W. Boyd, *Nat. Rev. Mater.* **2019**, *4*, 535.
- [18] J. Wu, Z. T. Xie, Y. Sha, H. Fu, Q. Li, *Photonics Res.* **2021**, *9*, 1616.
- [19] P. Jin, R. Ziolkowski, *IET Microw., Antennas propag.* **2010**, *4*, 1016.
- [20] Z. Li, S. Butun, K. Aydin, *ACS Photonics* **2015**, *2*, 183.
- [21] M. Heydari, M. Sabaeian, *Appl. Opt.* **2017**, *56*, 1917.
- [22] A. Imamog, D. D. Awschalom, G. Burkard, D. P. DiVincenzo, D. Loss, M. Sherwin, A. Small, *Phys. Rev. Lett.* **1999**, *83*, 4204.
- [23] A. D. Greentree, C. Tahan, J. H. Cole, L. C. Hollenberg, *Nat. Phys.* **2006**, *2*, 856.
- [24] A. Patra, V. Caligiuri, B. Zappone, R. Krahne, A. De Luca, *Nano Lett.* **2023**, *23*, 1489.
- [25] K. J. Vahala, *Nature* **2003**, *424*, 839.
- [26] F. Liang, N. Clarke, P. Patel, M. Loncar, Q. Quan, *Opt. Express* **2013**, *21*, 32306.
- [27] A. Frisk Kockum, A. Miranowicz, S. De Liberato, S. Savasta, F. Nori, *Nat. Rev. Phys.* **2019**, *1*, 19.
- [28] T. Herzog, S. Böhrkircher, S. Both, M. Fischer, R. Sittig, M. Jetter, S. Portalupi, T. Weiss, P. Michler, *Phys. Rev. B* **2020**, *102*, 235306.
- [29] K. C. Smith, Y. Chen, A. Majumdar, D. J. Masiello, *Phys. Rev. Appl.* **2020**, *13*, 044041.
- [30] T. Cui, B. Bai, H.-B. Sun, *Adv. Funct. Mater.* **2019**, *29*, 1806692.
- [31] I. De Bellis, D. Martella, C. Parmeggiani, D. S. Wiersma, S. Nocentini, *Adv. Funct. Mater.* **2023**, *33*, 2213162.
- [32] I. Zubrinskaya, R. Cicheler, I. Faniayeu, D. Martella, S. Nocentini, P. Rudquist, D. S. Wiersma, M. L. Brongersma, *Adv. Mater.* **2023**, *35*, 2209152.
- [33] M. Sharma, T. Ellenbogen, *Laser Photonics Rev.* **2020**, *14*, 2000253.
- [34] G. E. Lio, A. Ferraro, *Photonics* **2021**, *8*, 3.
- [35] J. Wang, K. Li, H. He, W. Cai, J. Liu, Z. Yin, Q. Mu, V. K. Hisao, D. Gérard, D. Luo, et al., *Laser Photonics Rev.* **2022**, 2100396.
- [36] G. Palermo, A. Lininger, A. Guglielmelli, L. Ricciardi, G. Nicoletta, A. De Luca, J.-S. Park, S. W. D. Lim, M. L. Meretska, F. Capasso, et al., *ACS Nano* **2022**, *16*, 16539.
- [37] R. Kowrdziej, J. Krupka, E. Nowinowski-Kruszelnicki, M. Olifierczuk, J. Parka, *Appl. Phys. Lett.* **2013**, *102*, 102904.
- [38] D. C. Zografopoulos, A. Ferraro, R. Beccherelli, *Adv. Mater. Technol.* **2019**, *4*, 1800447.
- [39] R. Kowrdziej, T. Stańczyk, J. Parka, *Liq. Cryst.* **2015**, *42*, 430.
- [40] G. Isić, G. Sinatkas, D. C. Zografopoulos, B. Vasić, A. Ferraro, R. Beccherelli, E. E. Kriezis, M. Belić, *IEEE J. Sel. Top. Quantum Electron.* **2019**, *25*, 1.
- [41] J. N. Israelachvili, P. M. McGuiggan, *J. Mater. Res.* **1990**, *5*, 2223.
- [42] B. Zappone, V. Caligiuri, A. Patra, R. Krahne, A. De Luca, *ACS Photonics* **2021**, *8*, 3517.
- [43] G. Fowles, *Modern optics*, Holt, New York **1989**.
- [44] M. Born, E. Wolf, *Principles of optics: electromagnetic theory of propagation, interference and diffraction of light*, Elsevier, Amsterdam **2013**.
- [45] R. Dkabrowski, P. Kula, J. Herman, *Crystals* **2013**, *3*, 443.
- [46] R. Węglowski, W. Piecek, A. Kozanecka-Szmigiel, J. Konieczkowska, E. Schab-Balcerzak, *Opt. Mater.* **2015**, *49*, 224.
- [47] W. Cai, V. M. Shalaev, *Optical Metamaterials*, vol. 10, Springer, Berlin **2010**.
- [48] M. Silveirinha, N. Engheta, *Phys. Rev. Lett.* **2006**, *97*, 157403.
- [49] V. Caligiuri, M. Palei, G. Biffi, R. Krahne, *Nanophotonics* **2019**, *8*, 1505.
- [50] J. Konieczkowska, E. Schab-Balcerzak, M. Siwy, K. Switkowski, A. Kozanecka-Szmigiel, *Opt. Mater.* **2015**, *39*, 199.
- [51] J. N. Israelachvili, P. M. McGuiggan, *J. Mater. Res.* **1990**, *5*, 2223.
- [52] J. N. Israelachvili, *Intermolecular and surface forces*, Academic press, Cambridge **2011**.